ACS OMEGA

Open Access

http://pubs.acs.org/journal/acsodf

Article

Nitrogen-Doped Carbon Nanothin Film as a Buffer Layer between Anodic Graphite and Solid Electrolyte Interphase for Lithium−Ion Batteries

Junzo Ukai, Kyusung Kim, Shinsuke Matsuhara, Li Yang, and Nagahiro Saito*

Cite This: *ACS Omega* 2024, 9, 24372−24378

Read Online

ACCESS | Metrics & More | Article Recommendations

ABSTRACT: Lithium−ion batteries are essential batteries for electric vehicle drive systems. Such batteries must provide stable performance over a long period of time. Therefore, the degradation or aging of the battery capacity must be improved. In the case of the current graphite anodes, graphite coated with an amorphous layer is used. It is known that the amorphous layer can reduce the irreversible capacity loss caused by the solid electrolyte interphase (SEI) layer. The amorphous carbon layers reduce the initial capacity due to higher electrical resistance. In this study, we aim to develop a buffer layer using nitrogen-containing graphene that would prevent the increase in electrical resistance while maintaining the amorphous structure. Coatings with different film thicknesses were prepared by using the solution plasma method. The thinnest sample was oven sintered to optimize the structure, especially the surface and interface of the layer. The battery capacity from charge−discharge experiments and the resistance change of each part from electrochemical impedance measurements were evaluated. The results showed that the coating layer increased the electrical resistance of the graphite anode. On the other hand, the resistance of the SEI layer was reduced by the coating layer. It can be predicted that the addition of the coating layer will increase the total charge transfer resistance (R_{ct}) of the cell but will also improve the period average capacity in the long run. To be used as a practical material, the film thickness would need to be further reduced, and the balance between the loss of charge transfer resistance and the gain of SEI layer resistance would need to be further optimized.

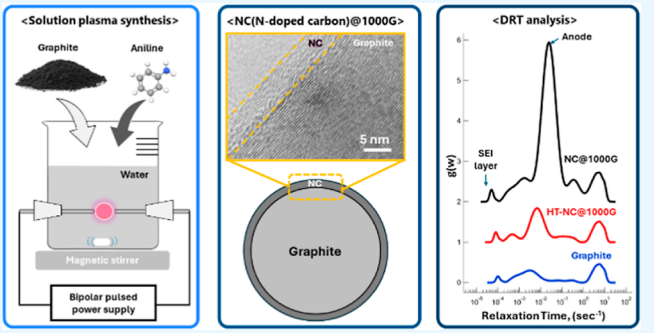

INTRODUCTION

Lithium−ion rechargeable batteries (LIBs) are used in many small portable devices, such as cell phones, and their performance is constantly improving. As LIBs are expected to become a power source for automobiles, there is a need to improve their characteristics, such as high capacity, low resistance, fast charging, and durability over many cycles.[1−5] In LIBs, lithium ions move from the positive electrode ($LiCoO_2$ or $LiMn_2O_4$ material) to the negative electrode (graphite material) through the electrolyte ($LiPF_6$ carbonate electrolyte) during charging. At the same time, electrons flow from the anode collector to the negative electrode and from the positive electrode to the positive electrode collector. The reverse process occurs during discharge. The search for cathode active materials has led to the development of high capacities. New active materials, such as silicon-based and tin-based materials, for the negative electrode are being researched and developed. However, these materials have a high volume expansion coefficient and have not surpassed graphite in terms of stability, durability, and cycling characteristics. From another perspective, it is extremely important for the negative electrode to minimize the degradation of durability and cycling characteristics due to solid electrolyte interphase (SEI) formation and graphite degradation.[6−21]

The SEI layer, which consists of lithium-based salts, lithium-based carbonates, and organic oligomers generated from the electrolyte, is formed on the graphite surface of the negative electrode. Its crystalline structure and thickness affect the charge transfer resistance (R_{ct}) and specific capacity.[22] Excess lithium accumulates on the graphite surface during charging and forms a SEI layer, which undergoes a surface oxidation reaction during discharging. The composition of the SEI layer is reported to be strongly influenced by the surface structure of the graphite.[23,24] On the basal surface of highly oriented pyrolytic graphite (HOPG), 18.5% of the SEI layer is

Received: December 30, 2023
Revised: February 11, 2024
Accepted: February 27, 2024
Published: May 30, 2024

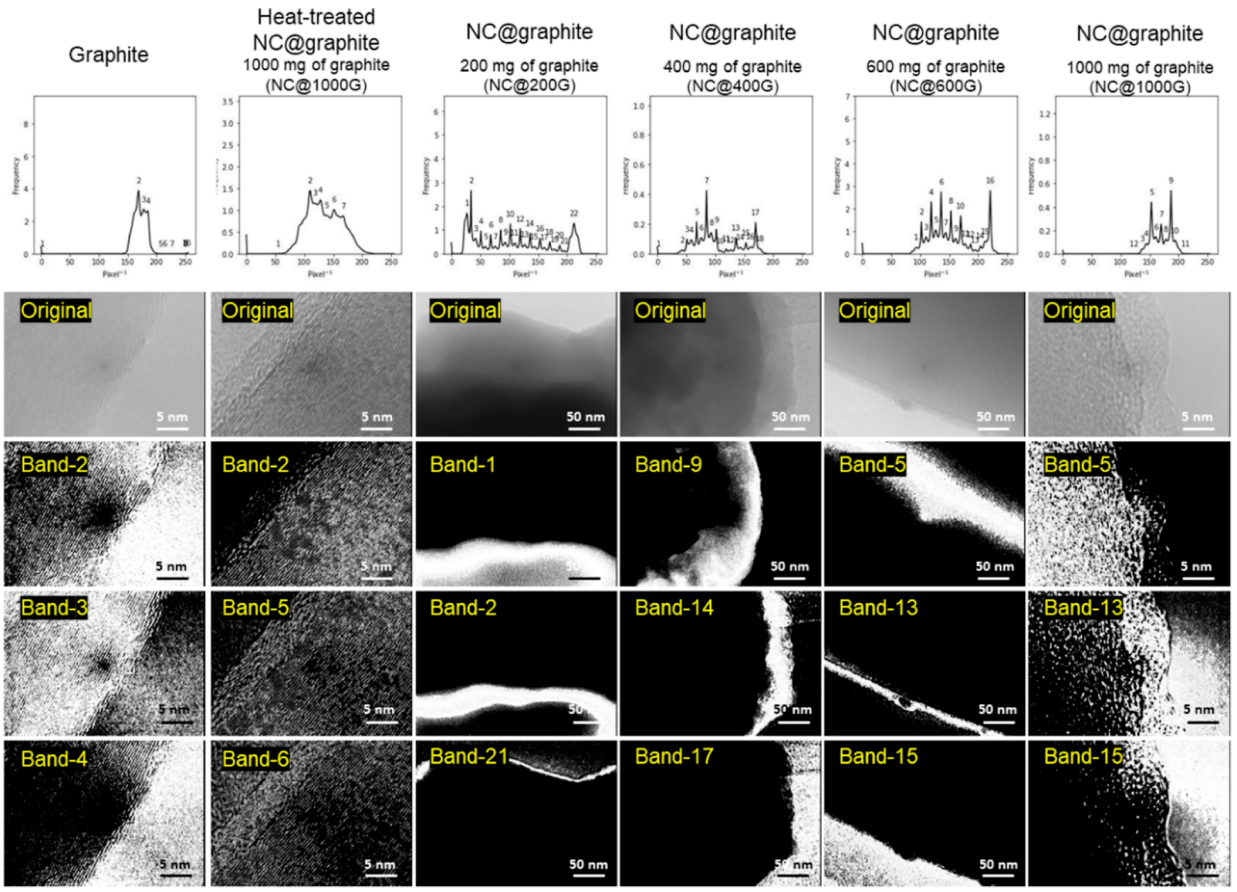

Figure 1. TEM images of graphite, SP-treated nitrogen-containing carbon-coated graphite (NC@200G, NC@400G, NC@600G, and NC@1000G), and HT-NC@1000G samples with heat-treated NC@1000G; histogram plots of spatial frequency analysis; and band images of characteristic frequency bands. Here, the numbers in the histograms indicate the band numbers.

composed of lithium-based salts, compared to 69.4% on the cross-section of HOPG, 47.5% on soft carbon, and 60.3% on hard carbon. Insoluble lithium-based carbonates are present only on the basal surface of the HOPG and account for 22.8% of the SEI layer.[25] The insoluble SEI component is responsible for the irreversible capacity loss. To prevent this, amorphous carbon is currently used as a buffer layer a few nanometers thick around graphite to suppress the formation of insoluble SEI components and prevent irreversible capacity increases. However, the amorphous carbon buffer layer also increases the charge transfer resistance, resulting in an energy loss. Therefore, as an alternative to the amorphous carbon buffer layer, it is necessary to develop a buffer layer with a low electrical resistance that can avoid the formation of insoluble SEI components.

The size of graphite crystallites can be determined by the dimensions parallel to the *a* and *c* axes (called L_a and L_c, respectively). L_a represents the extent of the basal plane, the 002 plane; L_c is a group of planes representing the layered cross-section. For hard carbon and graphite, the L_c/L_a ratio is about 0.5, and for soft carbon, it is about 1.[26,27] Carbon materials with L_a greater than L_c have an advantage in the intercalation reaction of lithium ions because the proportion of interlayer sites appearing on the surface increases. However, the interlayer sites are unstable, in terms of surface energy, and are the sites where the formation of insoluble SEI layers is likely to occur. Therefore, to take advantage of these structures, which are superior to the intercalation reaction of carbon, it is essential to develop carbon coatings that minimize the decrease in electrical resistivity while suppressing the formation of SEI layers.[28]

Our research group found that nitrogen-doped carbon-coated carbon nanotubes successfully reduced the electrical resistivity of CNT thin films by using the solution plasma (SP) method with aniline as a raw material.[29] Furthermore, when using SP to synthesize graphene and nitrogen-containing graphene, they found that nitrogen is the end point of the six-membered ring formation reaction when prepared from nitrogen-containing raw materials, resulting in a smaller crystallite size.[30]

In this study, we aimed to utilize the research results to nanocoated nitrogen-containing carbon as a buffer layer with a small crystallite size and low electrical resistance. The thickness of the thin film was adjusted by optimizing the amount of graphite precursor added, and the nitrogen-containing carbon films were compared by heat treatment to control their crystallinity. The thickness of the thin film was adjusted by optimizing the amount of graphite precursor added, and the crystallinity of the nitrogen-containing carbon film was controlled by heat treatment for comparison. The surface of the nitrogen-containing carbon buffer layer was observed by transmission electron microscopy, and the periodicity of the carbon structure was evaluated by Raman spectroscopy. Finally, coin cells were assembled, and their capacities were evaluated by charge−discharge experiments. Electrochemical impedance measurements were used to determine the charge

https://doi.org/10.1021/acsomega.3c10502
ACS Omega 2024, 9, 24372−24378

transfer resistance. Three types of cells were compared in this study: graphite, graphite coated with a nitrogen-containing carbon buffer layer deposited with SP, and graphite coated with a nitrogen-containing carbon buffer layer that was heat-treated.

EXPERIMENTAL SECTION

Aniline ($C_6H_5NH_2$) of 99.0% purity, hydrochloric acid (HCl) solution of 35.0 to 37.0% concentration, *N*-methyl-2-pyrrolidinone (NMP) of 99.0% purity, and sulfuric acid (H_2SO_4) of 0.5 M concentration were purchased from Kanto Chemicals. 34.5% hydrogen peroxide (H_2O_2) was purchased from Wako Chemicals Co. The graphite core of the LIBs was purchased from Wako Chemicals, Inc. Spheroidized natural graphite (CGB-10: Nippon Graphite Industry Co., Ltd.) was used for the graphite core of the LIB. All chemicals were undiluted. An Aquarius water purification system (RFD250NB, Advantech, Japan) was used to obtain ultrapure water of 18.2 MΩ•cm at 25 °C. 125 mL of 1 M HCl, 1.25 mL of aniline, and 200, 400, 600, and 1000 mg of graphite were added to 30 mL of ultrapure water and 200 mL in a glass vessel, and the mixture was stirred for 15 min to homogenize. The mixture was then dispersed using a probe-type ultrasonic homogenizer (Sonifier model 450: Branson) at a 15 W output for 15 min to obtain a uniform graphite-aniline solution without surfactant. A predetermined amount of graphite-aniline solution was poured into the synthetic SP reaction vessel shown in Figure 1, which illustrates the experimental setup for SP. A 1 mm diameter nickel (Ni, 99.99% purity: Nilaco) wire electrode was shielded with ceramic tube insulation and placed in the SP reactor with a distance of 0.5 mm between electrodes. A bipolar pulse power supply (MPP-HV04: Kurita Water Industries) was used to generate and maintain SP in the mixture. The voltage applied between the electrodes was maintained at a repetition frequency of 45 kHz and a pulse width of 1.3 μs to generate the plasma for 15 min. Plasma was generated by applying a pulse voltage between the terminals in a stirred aqueous solution. After plasma generation, the temperature of the aqueous solution was maintained at room temperature. After plasma treatment, 60 mL of a 6 wt % H_2O_2 solution was added to this solution to neutralize it, and the solution was left in this state for 6 h. The synthetic sample was then vacuum filtered through a polytetrafluoroethylene (PTFE) membrane filter (pore size of 0.1 mm, JVWP04700, Merck Millipore). After filtration, the samples were thoroughly washed with distilled water and 1.0 M KOH and dried in a vacuum oven at 60 °C for 3 h.

The dried samples were ultrasonically dispersed by immersion in ethanol for 10 min. The resulting graphite-ethanol solution was applied to a TEM grid, and the coating layer was observed at high resolution by TEM (JEM-2500SE, JEOL) and STEM-EDS (acceleration voltage of 200 kV). Structural analysis was performed using a SmartLab X-ray diffractometer (Rigaku) with a CuKα source, an acceleration voltage of 45 kV, and a current of 200 mA. Diffraction angles (2θ) ranged from 10 to 80°, the scan speed was 2.4° min^{-1}, and diffraction patterns were obtained with a step size of 0.02, a 0.5° distribution slit, a 0.5° scattering slit, and a 0.15 mm receiving slit. The near-surface ring structure of carbon was evaluated by Raman spectroscopy (InVia Qontor, Renishaw). Raman spectra were collected in the wavenumber range 100−3000 cm^{-1} using a laser excitation wavelength of 532.5 nm. Five exposures of 10 s each were taken at room temperature and averaged.

The manufacturing conditions of the battery cells were as follows. NCM (nickel manganese cobalt lithium oxide) was used as the cathode active material, and polyethylene was used as the separator. The electrolyte was a mixture of EC (ethylene carbonate) and EMC (ethyl methyl carbonate) with $LiPF_6$ at 3:7, and the concentration was adjusted to 1.1 M. For the cathode, NCM, PVDF (polyvinylidene fluoride), and CB (carbon black) were added to the NMP solution to form a slurry, which was applied in fixed amounts and rolled to a density of 2.5 g/cm^3. Graphite, SP-coated graphite, and SP-coated heat-treated graphite were used as the anode active materials, respectively, and CMC (carboxymethyl cellulose) was added and mixed with distilled water, and SBE was added to form a slurry. A certain amount of this slurry was applied and rolled to a final density of 1.3 g/cm^3. The cell was assembled into a pouch cell. After the cathode, anode, and separator were assembled, the cell was dried at 100 °C for 12 h and filled with electrolytes. The cells were then charged to 4.1 V at a constant current and voltage (CCCV) of 0.5 °C, discharged to 3.0 V at a constant current and voltage of 0.5 °C, and charged and discharged three times between 3 and 4.1 V to activate the cells. Capacity measurements were performed on batteries that had undergone this activation process. The capacity measurement conditions were as follows: the battery was prepared, discharged to 3.0 V, charged to 4.1 V at a rate of 0.2 °C, paused for 10 min, and then CCCV discharged to 3.0 V at a rate of 0.2 °C. The nominal capacity of the battery was the discharge capacity at this time. Impedance measurements were made at 0 °C, 60% state of charge, 5 mV amplitude, and 105−10−2 Hz after the capacity measurement. An impedance analyzer (Toyo Technica, model 1255b) was used for the electrochemical measurements described above, and a charge/discharge measurement system (BCS series, BioLogic Science Instruments) was used for the charge/discharge experiments.

RESULTS AND DISCUSSION

Graphite samples of 200, 400, 600, and 1000 mg were placed in a fixed volume of solution and treated with SP. Each of the resulting samples and untreated graphite were observed by TEM. Figure 1 shows the TEM of graphite of 200, 400, 600, and 1000 mg, each of which was placed in the solution and treated with SP (referred to as NC@200G, NC@400G, NC@

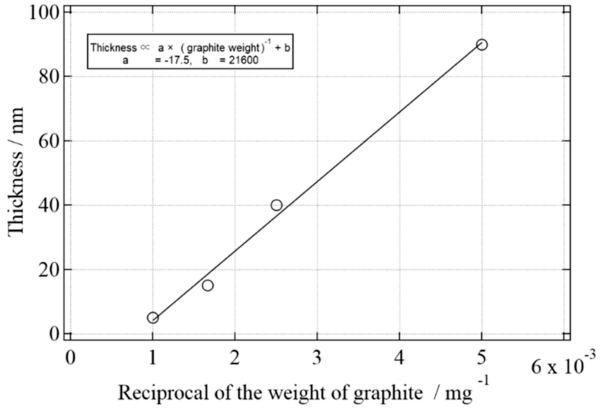

Figure 2. Relationship between the reciprocal amount of graphite added and the thickness of the coating layer.

https://doi.org/10.1021/acsomega.3c10502
ACS Omega 2024, 9, 24372−24378

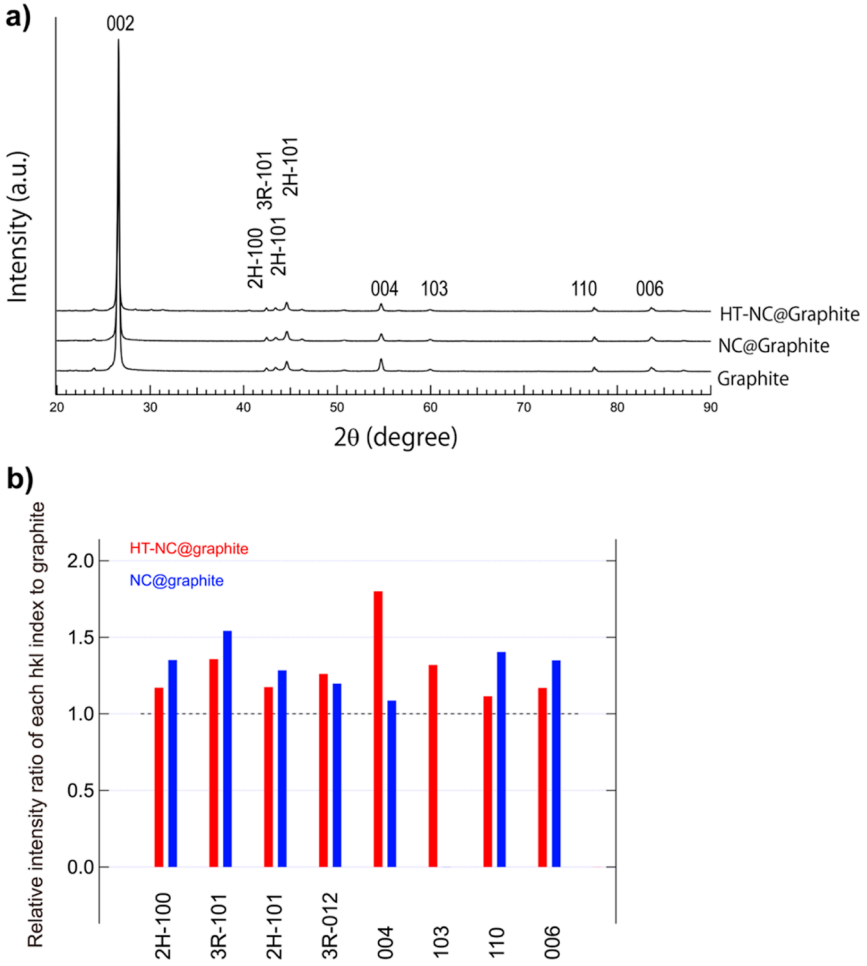

Figure 3. (a) X-ray diffraction patterns of the graphite, NC@1000G, and HT-NC@1000G samples and (b) the changes in the relative intensity ratio of each hkl index between the samples.

600G, and NC@1000G, respectively), and a sample of NC@1000G that was heat-treated (referred to as HT-NC@1000G). The figure is labeled original. From these images, no contrast change can be observed at the interface in the graphite itself, but a contrast change can be observed in the images with the coating layer. To partition the graphite core and the coating layer according to structural differences, a spatial Fourier transform was performed, and the partitioning was done according to structural features. First, the image size was standardized to 3600 × 2600 pixels, a two-dimensional Fourier transform was performed to derive the spatial frequency, and the image was decomposed into images in each band by defining a frequency band at ±10 (1/pixel) from the characteristic frequency peak. A histogram is also displayed to illustrate the spatial frequency data. The histogram displays the frequency on the *y*-axis and the reciprocal number of pixels on the *x*-axis. In this case, the *x*-axis corresponds to the spatial frequency under the conditions of the image resolution determined by the image processing, as described above. Figure 1 shows the characteristic band images for each original image. The smaller the number of bands, the lower the spatial frequency, and the larger the number of bands, the higher the spatial frequency. For each sample, the low-frequency band image, the midfrequency band image, and the high-frequency band image are in this order. The high-frequency side and the low-frequency side change relative to the graphite inside side and the TEM mesh side, but the graphite interface region is characteristically extracted in the midfrequency band image. The area was estimated from this midfrequency band image, and the average thickness of the coating layer was calculated. As a result, the average film thicknesses of NC@200G, NC@400G, NC@600G, NC@1000G, and HT-NC@1000G were found to be 90, 40, 15, 5, and 4 nm, respectively.

The relationship between film thickness and the inverse of the graphite weight input during SP treatment is shown in Figure 2. Assuming a uniform graphite diameter, this input is proportional to the particle concentration since the solution volume is constant. Therefore, the inverse will be linear with the plasma treatment time (residence time) per particle. From the graph, the inverse relationship between the graphite weight and film thickness can be approximated by a linear equation. This means that the rate of carbon deposition by SP is constant

$$\text{Thickness} = -17.5\left(\frac{1}{w_g}\right) + 21600 \quad (1)$$

In Figure 3a, XRD analysis of graphite, NC@graphite, and HT-NC@graphite was performed to evaluate the degree of crystallinity relative to the bulk. Each reflection is assigned to graphite 002, 2H-100, 3R101, 3R-012, 004, 013, 110, and 006 from the low angle side. From these data, relative intensities were obtained by dividing the intensity of each hkl index by the

https://doi.org/10.1021/acsomega.3c10502
ACS Omega 2024, 9, 24372−24378

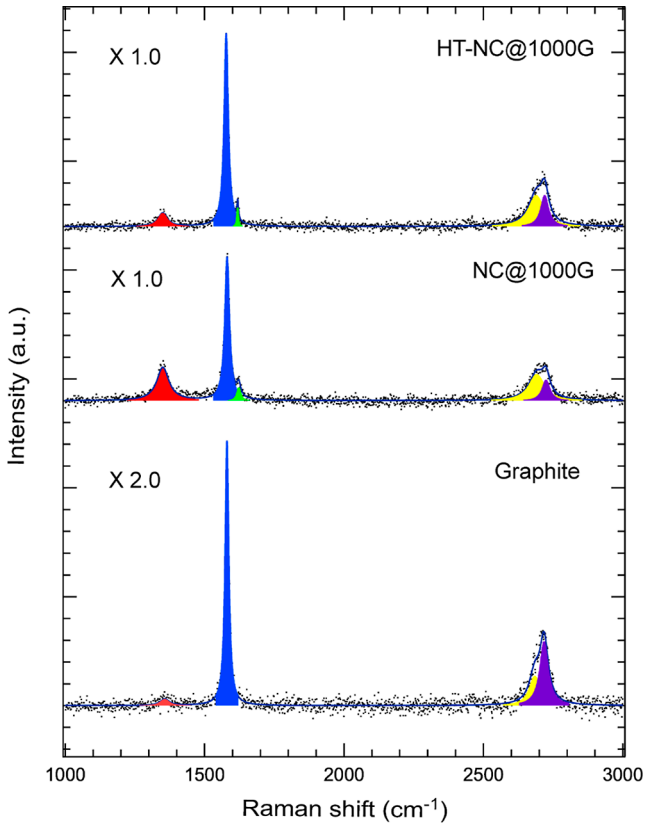

Figure 4. Raman spectra and Gaussian deconvolution of graphite, NC@1000G, and HT-NC@1000G.

intensity of the 002 reflection within each sample as an internal standard, as shown in Figure 3b. For comparison between samples, the relative intensity of each hkl index was obtained by dividing the relative intensity of each hkl index in the other sample by the relative intensity of each hkl index in graphite. To examine the variability of I_{004}, the I_{004}/I_{002} ratio was used. The I_{004}/I_{002} ratios within each sample were 0.048, 0.046, and 0.049, with HT-NC@ graphite slightly exceeding graphite. Inagaki et al.[31] also reported the relationship between the I_{004}/I_{002} ratio and heating temperature and the I_{004}/I_{002} ratio and *c*-axis direction. According to them, a heating temperature of 500 °C or higher is required for an I_{004}/I_{002} ratio of 0.048. The *d*-spacing is 3.45 Å, which results in graphite with a wide 002 plane spacing between layers. The present results show no significant change in the intensity of I_{004} with heat treatment, indicating that graphite is partially moving toward graphitization but still has an amorphous structure.

The Raman analysis of graphite, nitrogen-doped graphite, and high-temperature nitrogen-doped graphite is shown in Figure 4, where the D band is shown in red, the G band is shown in blue, the D band is shown in green, the $2D_1$ band is shown in yellow, and the $2D_2$ band is shown in purple. The I_D/I_G ratios of the samples were 0.06, 0.62, and 0.15, respectively. These results suggest that the bonding between the six-membered rings in the deposited layer has progressed due to the heat treatment: the 2D band of graphene formed by the bonding of the six-membered rings is an overtone of the D band; as the ratio of the G band capitals increases, the planarity and π-conjugation broaden; and the $2D_2$ band is used to evaluate the I_{2D}/I_G ratios for the three samples, which were determined to evaluate carbon in LIBs and were 0.58, 0.24, and 0.30, respectively.[32,33] The value for the graphite sample was 0.58, which represents only the graphite material. On the other hand, the value of 0.24 identifies the graphite material and the structure of the deposited layer. On the other hand, the value of 0.24 reflects the structure of the graphite material and the deposited layer. Interestingly, the NC@ graphite sample shows a significantly lower ratio than the graphite sample, despite the minimal thickness of the deposited layer. This indicates that the measurement is more sensitive to the near-surface structure and mainly detects the structure of the deposited layer: for NC@1000G, the ratio is 0.30, which is similar to the value for graphite. However, the 2D structure of the deposited layer still contains a significant amount of an amorphous structure.

The charge−discharge experiments showed that the graphite was 16.0, 14.3, and 15.0 mA/g for graphite, NC@1000G, and HT-NC@1000G. As a result, the capacitance decreased for the SP-coated graphite, while the capacitance decrease was

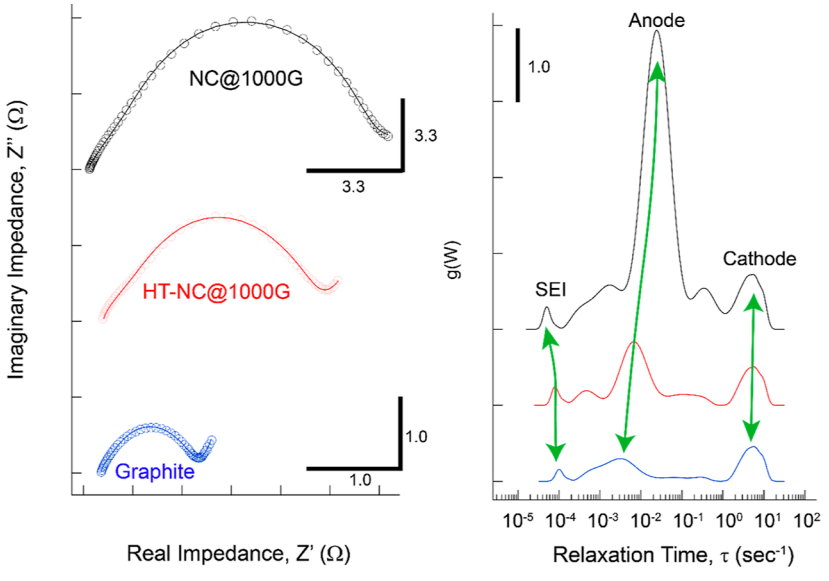

Figure 5. Nyquist plot and DRT analysis based on electrochemical impedance.

https://doi.org/10.1021/acsomega.3c10502
ACS Omega 2024, 9, 24372−24378

suppressed for the heat-treated graphite. In both cases, it can be said that the capacitance decreased due to the increase in electrical resistance. Nyquist plots of electrochemical impedance [34−34] and relaxation time distribution (DRT) analysis[35−37] are shown in Figure 5. As can be seen from the Nyquist plots, the increase in RCT is clearly indicated, as mentioned above. Peak (1), which appears at a short relaxation time, is the response of the SEI layer; peak (2) is the response of the anode; and peak (3) is the response of the cathode. The two minor peaks located near peak (2) were related coating layers. The variation of peak (3) is smaller than that of the original graphite. On the other hand, peak (2) shows a shift toward a longer relaxation time, indicating that the addition of the coating layer to the graphite increases the resistance and decreases the capacitance. Peak (1), on the other hand, shows a shift toward shorter relaxation times, indicating that the presence of the coating layer decreases the resistance of the SEI layer. This implies an irreversible decrease in the capacitance loss. Therefore, although the initial capacity performance of the battery is reduced by the coating layer, the irreversible capacity loss is also reduced, thereby reducing the capacity variations during long-term use. In actual batteries, at least an even thinner coating layer than that deposited in this study should be used to reduce the electrical resistance in order to optimize the balance between the initial capacity reduction and the reduction of the capacity variation during long-term use. In addition, XRD and Raman analysis results showed partial graphitization of the coating layer, but an amorphous structure still remained; therefore, it is expected that optimization will be made in the direction of increasing the percentage of graphitization within the coating layer.

CONCLUSIONS

In this study, graphite samples were coated with nitrogen-containing graphene at different film thicknesses using the SP method. XRD analysis showed that the coating layer also changed to a graphite-like structure after heat treatment based on the I_{004}/I_{002} ratio, but only partially. Raman analysis also showed that the graphite after heat treatment still contained a sufficient amount of amorphous structure, although it approached graphite values. However, the heat treatment significantly improved the electrical conductivity, although the amorphous structure was retained. In charge−discharge experiments, the resistance of graphite with the heat-treated coating layer was significantly reduced compared to that before heat treatment, approaching the resistance of graphite itself. However, even with this improved resistance, a decrease in the initial battery capacity was observed. Electrochemical impedance measurements showed that the battery capacity decreased as the RCT increased. This increase in the RCT is due to the coating layer. In fact, DRT analysis showed that graphite with the coating layer showed an increase in electrical resistance. On the other hand, the resistance of the SEI layer decreased due to the coating layer. This means that the actual capacitance is expected to improve in the long run. Further improvements are needed to reduce the film thickness and increase the graphitization ratio within the coating layer in order to use it as a practical material.

AUTHOR INFORMATION

Corresponding Author

Nagahiro Saito − *Department of Chemical Systems Engineering, Graduate School of Engineering, Nagoya University, Chikusa-ku, Nagoya 464-8603, Japan; Institute of Material Innovation, Institutes of Innovation for Future Society, Nagoya University, Nagoya 464-8601, Japan; Department of International Collaborative Program in Sustainable Materials and Technology for Industries Between Nagoya University and Chulalongkorn University, Graduate School of Engineering, Nagoya University, Chikusa-ku, Nagoya 464-8603, Japan; Conjoint Research Laboratory in Nagoya University, Shinshu University, Chikusa-ku, Nagoya 464-8603, Japan;* orcid.org/0000-0001-8757-3933; Email: hiro@sp.material.nagoya-u.ac.jp

Authors

Junzo Ukai − *Department of Chemical Systems Engineering, Graduate School of Engineering, Nagoya University, Chikusa-ku, Nagoya 464-8603, Japan*

Kyusung Kim − *Institute of Material Innovation, Institutes of Innovation for Future Society, Nagoya University, Nagoya 464-8601, Japan*

Shinsuke Matsuhara − *Toyota Motor Corporation, Toyota-cho, Toyota 471-8571, Japan*

Li Yang − *Frontiers Science Center for Transformative Molecules, School of Chemistry and Chemical Engineering, Shanghai Jiao Tong University, Shanghai 200240, China;* orcid.org/0000-0003-2334-1206

Complete contact information is available at: https://pubs.acs.org/10.1021/acsomega.3c10502

Notes

The authors declare no competing financial interest.

ACKNOWLEDGMENTS

We would like to acknowledge financial support from the Japan Science and Technology Agency, Strategic International Collaborative Research Program (Grant no. JPMJSC18H1).

REFERENCES

(1) Ibrahim, H.; Ilinca, A.; Perron, J. Energy storage systems-Characteristics and comparisons. *Renewable Sustainable Energy Rev.* **2008**, *12*, 1221−1250.

(2) Raj, B.; Sahoo, M. K.; Nikoloski, A.; Singh, P.; Basu, S.; Mohapatra, M. Retrieving Spent Cathodes from Lithium-Ion Batteries through Flourishing Technologies. *Batteries Supercaps* **2023**, *6*, No. e202200418.

(3) Li, M.; Lu, J.; Chen, Z.; Amine, K. 30 Years of Lithium-Ion Batteries. *Adv. Mater.* **2018**, *30*, 1800561.

(4) Etacheri, V.; Marom, R.; Elazari, R.; Salitra, G.; Aurbach, D. Challenges in the development of advanced Li-ion batteries: A review. *Energy Environ. Sci.* **2011**, *4*, 3243−3262.

(5) Kim, T.; Song, W.; Son, D. Y.; Ono, L. K.; Qi, Y. Lithium-ion batteries: outlook on present, future, and hybridized technologies. *J. Mater. Chem. A Mater.* **2019**, *7*, 2942−2964.

(6) Deng, D. Li-ion batteries: Basics, progress, and challenges. *Energy Sci. Eng.* **2015**, *3*, 385−418.

(7) Zhang, Q.; Pan, J.; Lu, P.; Liu, Z.; Verbrugge, M. W.; Sheldon, B. W.; Cheng, Y. T.; Qi, Y.; Xiao, X. Synergetic Effects of Inorganic Components in Solid Electrolyte Interphase on High Cycle Efficiency of Lithium Ion Batteries. *Nano Lett.* **2016**, *16*, 2011−2016.

(8) Hardwick, L. J.; Marcinek, M.; Beer, L.; Kerr, J. B.; Kostecki, R. An Investigation of the Effect of Graphite Degradation on Irreversible Capacity in Lithium-ion Cells. *J. Electrochem. Soc.* **2008**, *155*, A442.

(9) Luo, J.; Wu, C. E.; Su, L. Y.; Huang, S. S.; Fang, C. C.; Wu, Y. S.; Chou, J.; Wu, N. L. A proof-of-concept graphite anode with a lithium dendrite suppressing polymer coating. *J. Power Sources* **2018**, *406*, 63−69.

https://doi.org/10.1021/acsomega.3c10502
ACS Omega 2024, 9, 24372−24378

(10) Waldmann, T.; Hogg, B. I.; Wohlfahrt-Mehrens, M. Li plating as unwanted side reaction in commercial Li-ion cells − A review. *J. Power Sources* **2018**, *384*, 107−124.
(11) Björklund, E.; Xu, C.; Dose, W. M.; Sole, C. G.; Thakur, P. K.; Lee, T. L.; De Volder, M. F. L.; Grey, C. P.; Weatherup, R. S. Cycle-Induced Interfacial Degradation and Transition-Metal Cross-Over in LiNi0.8Mn0.1Co0.1O2-Graphite Cells. *Chem. Mater.* **2022**, *34*, 2034−2048.
(12) Xiong, Y.; Liu, Y.; Chen, L.; Zhang, S.; Zhu, X.; Shen, T.; Ren, D.; He, X.; Qiu, J.; Wang, L.; Hu, Q.; Zhang, H. New Insight on Graphite Anode Degradation Induced by Li-Plating. *Energy Environ. Mater.* **2022**, *5*, 872−876.
(13) Jiang, M.; Danilov, D. L.; Eichel, R. A.; Notten, P. H. L. A Review of Degradation Mechanisms and Recent Achievements for Ni-Rich Cathode-Based Li-Ion Batteries. *Adv. Energy Mater.* **2021**, *11*, 2103005.
(14) Ushirogata, K.; Sodeyama, K.; Futera, Z.; Tateyama, Y.; Okuno, Y. Near-Shore Aggregation Mechanism of Electrolyte Decomposition Products to Explain Solid Electrolyte Interphase Formation. *J. Electrochem. Soc.* **2015**, *162*, A2670−A2678.
(15) Cai, W.; Yao, Y. X.; Zhu, G. L.; Yan, C.; Jiang, L. L.; He, C.; Huang, J. Q.; Zhang, Q. A review on energy chemistry of fast-charging anodes. *Chem. Soc. Rev.* **2020**, *49*, 3806−3833.
(16) Wu, Y.; Zhao, H.; Wu, Z.; Yue, L.; Liang, J.; Liu, Q.; Luo, Y.; Gao, S.; Lu, S.; Chen, G.; Shi, X.; Zhong, B.; Guo, X.; Sun, X. Rational design of carbon materials as anodes for potassium-ion batteries. *Energy Storage Mater.* **2021**, *34*, 483−507.
(17) Zhang, J.; Wu, J. F.; Wang, Z.; Mo, Y.; Zhou, W.; Peng, Y.; He, B.; Xiao, K.; Chen, S.; Xu, C.; Liu, J. Stabilizing SEI by cyclic ethers toward enhanced K+ storage in graphite. *J. Energy Chem.* **2022**, *71*, 344−350.
(18) Xiao, K.; Wu, J. F.; Yan, H.; Mo, Y.; Zhou, W.; Peng, Y.; Chen, S.; Cui, X.; Chen, L.; Xu, C.; Liu, J. Intercalation-deposition mechanism induced by aligned carbon fiber toward dendrite-free metallic potassium batteries. *Energy Storage Mater.* **2022**, *51*, 122−129.
(19) Sun, C.; Ji, X.; Weng, S.; Li, R.; Huang, X.; Zhu, C.; Xiao, X.; Deng, T.; Fan, L.; Chen, L.; Wang, X.; Wang, C.; Fan, X. 50C Fast-Charge Li-Ion Batteries using a Graphite Anode. *Adv. Mater.* **2022**, *34*..
(20) Wu, J. F.; Zhou, W.; Wang, Z.; Wang, W. W.; Lan, X.; Yan, H.; Shi, T.; Hu, R.; Cui, X.; Xu, C.; He, X.; Mao, B. W.; Zhang, T.; Liu, J. Building K−C Anode with Ultrahigh Self-Diffusion Coefficient for Solid State Potassium Metal Batteries Operating at −20 to 120 °C. *Adv. Mater.* **2023**, *35*, 209833.
(21) Wu, J. F.; Zou, Z.; Pu, B.; Ladenstein, L.; Lin, S.; Xie, W.; Li, S.; He, B.; Fan, Y.; Pang, W. K.; Wilkening, H. M. R.; Guo, X.; Xu, C.; Zhang, T.; Shi, S.; Liu, J. Liquid-Like Li-Ion Conduction in Oxides Enabling Anomalously Stable Charge Transport across the Li/Electrolyte Interface in All-Solid-State Batteries. *Adv. Mater.* **2023**, *35*, 2303730.
(22) Wang, G.; Yu, M.; Feng, X. Carbon materials for ion-intercalation involved rechargeable battery technologies. *Chem. Soc. Rev.* **2021**, *50*, 2388−2443.
(23) An, S. J.; Li, J.; Daniel, C.; Mohanty, D.; Nagpure, S.; Wood, D. L. The state of understanding of the lithium-ion-battery graphite solid electrolyte interphase (SEI) and its relationship to formation cycling. *Carbon* **2016**, *105*, 52−76.
(24) Yu, X.; Jiang, Z.; Yuan, R.; Song, H. A Review of the Relationship between Gel Polymer Electrolytes and Solid Electrolyte Interfaces in Lithium Metal Batteries. *Nanomaterials* **2023**, *13*, 1789.
(25) Zhao, X.; Chen, Y.; Sun, H.; Yuan, T.; Gong, Y.; Liu, X.; Chen, T. Impact of Surface Structure on SEI for Carbon Materials in Alkali Ion Batteries: A Review. *Batteries* **2023**, *9*, 226.
(26) Moon, J.; Yun, H.; Ukai, J.; Chokradjaroen, C.; Thiangtham, S.; Hashimoto, T.; Kim, K.; Sawada, Y.; Saito, N. Correlation function of specific capacity and electrical conductivity on carbon materials by multivariate analysis. *Carbon* **2023**, *215*, 118479.
(27) Xie, L.; Tang, C.; Bi, Z.; Song, M.; Fan, Y.; Yan, C.; Li, X.; Su, F.; Zhang, Q.; Chen, C. Hard Carbon Anodes for Next-Generation Li-Ion Batteries: Review and Perspective. *Adv. Energy Mater.* **2021**, *11*, 2101650.
(28) Peled, E.; Menkin, S. Review—SEI: Past, Present and Future. *J. Electrochem. Soc.* **2017**, *164*, A1703−A1719.
(29) Chae, S.; Phan, P. Q.; Panomsuwan, G.; Bratescu, M. A.; Hashimoto, T.; Teshima, K.; Saito, N. Single-walled carbon nanotubes wrapped by cationic nitrogen-doped carbon for electrocatalytic applications. *ACS Appl. Nano Mater.* **2020**, *3*, 10183−10189.
(30) Kim, K.; Chokradjaroen, C.; Saito, N. Solution plasma: new synthesis method of N-doped carbon dots as ultra-sensitive fluorescence detector for 2,4,6-trinitrophenol. *Nano Express* **2020**, *1*, 020043.
(31) Inagaki, M.; Oberlin, A.; Noda, T. Structural Changes of Graphitizing Carbons during Graphitization*1-Review. *TANSO* **1975**, *1975*, 68−72.
(32) Wang, X.; Christopher, J. W.; Swan, A. K. 2D Raman band splitting in graphene: Charge screening and lifting of the K-point Kohn anomaly. *Sci. Rep.* **2017**, *7*, 13539.
(33) Neumann, C.; Reichardt, S.; Venezuela, P.; et al. Raman spectroscopy as probe of nanometre-scale J, Energy Chem., T. Momma, D. Mukoyama, H. Nara, Proposal of novel equivalent circuit for electrochemical impedance analysis of commercially available lithium ion battery. *J. Power Sources* **2012**, *205*, 483−486.
(34) Huang, J.; Sullivan, N. P.; Zakutayev, A.; O'Hayre, R. How reliable is distribution of relaxation times (DRT) analysis? A dual regression-classification perspective on DRT estimation, interpretation, and accuracy. *Electrochim. Acta* **2023**, *443*, 141879.
(35) Alavi, S. M. M.; Birkl, C. R.; Howey, D. A. Time-domain fitting of battery electrochemical impedance models. *J. Power Sources* **2015**, *288*, 345−352.
(36) Zheng, Y.; Shi, Z.; Guo, D.; Dai, H.; Han, X. A simplification of the time-domain equivalent circuit model for lithium-ion batteries based on low-frequency electrochemical impedance spectra. *J. Power Sources* **2021**, *489*, 229505.
(37) Kobayashi, K.; Suzuki, T. S. Extended Distribution of Relaxation Time Analysis for Electrochemical Impedance Spectroscopy. *Electrochemistry* **2022**, *90*, 017004.

https://doi.org/10.1021/acsomega.3c10502
ACS Omega 2024, 9, 24372−24378